Laser-Direct-Drive Fusion Target Design with a High-*Z* Gradient-Density Pusher Shell

S. X. Hu,[1,2,3,*] L. Ceurvorst,[1] J. L. Peebles,[1] A. Mao,[4] P. Li,[4] Y. Lu,[4] A. Shvydky,[1] V. N. Goncharov,[1,2] R. Epstein,[1] K. Nichols,[1,3] R. M. N. Goshadze,[1,3] M. Ghosh,[1] J. Hinz,[1,3] V. V. Karasiev,[1] S. Zhang,[1] N. R. Shaffer,[1] D. I. Mihaylov,[1] J. Cappelletti,[1,2] D. R. Harding,[1] C. K. Li,[5] E. M. Campbell,[6] R. C. Shah,[1] T. J. B. Collins,[1] S. P. Regan,[1,2] and C. Deeney[1]

[1]Laboratory for Laser Energetics, University of Rochester,
250 E. River Road, Rochester, NY 14623, USA
[*]shu@lle.rochester.edu

[2]Department of Mechanical Engineering, University of Rochester, Rochester, NY 14627, USA

[3]Department of Physics and Astronomy, University of Rochester, Rochester, NY 14627, USA

[4]Department of Electrical and Computer Engineering, University of Nebraska - Lincoln, Lincoln, NE 68588, USA

[5]Plasma Science and Fusion Center, Massachusetts Institute of Technology, 77 Massachusetts Avenue, Cambridge, Massachusetts 02139, USA

[6]MCM Consulting, San Diego, CA 97127, USA

ABSTRACT

Laser-direct-drive (LDD) fusion target designs, with solid deuterium-tritium (DT) fuel and a high-Z gradient-density pusher shell (GDPS) plus an Au-coated foam layer, have been investigated through both one-dimensional (1-D) and two-dimensional (2-D) radiation-hydrodynamic simulations. Compared with conventional low-Z ablators and *DT-push-on-DT* targets, these GDPS targets possess certain advantages of being less-demanded implosions that can be high-adiabat ($\alpha \geq 8$), low-convergence ($CR_{hs} \approx 22$ and $CR_{PS} \approx 17$), and low implosion velocity ($v_{imp} < 3 \times 10^7$ cm/s). Using symmetric drive with laser energies of 1.9 – 2.5 MJ, one-dimensional *LILAC* simulations of these GDPS implosions can give neutron yields corresponding to energy >~50 MJ even with a reduced laser absorption due to cross-beam energy transfer (CBET) effect. Two-dimensional *DRACO* simulations show these GDPS targets can still ignite and deliver up to ~10 MJ neutron yields even if CBET is present, while traditional *DT-push-on-DT* targets normally fail due to CBET-induced reduction of ablation pressure. If CBET is mitigated, these GDPS targets are expected to produce neutron yields of >20 MJ at a driven laser energy of ~2 MJ. The key factors behind the robust ignition and moderate energy gain of such GDPS implosions are: (1) The high initial density of the high-Z pusher shell can be placed on a very high adiabat, while the DT fuel is maintained in relatively low entropy state; such implosions can still provide enough compression $\rho R > 1$ g/cm^2 for sufficient confinement; (2) The high-Z layer significantly reduces heat conduction loss from the hot spot, as thermal conductivity scales as ~1/Z; and (3) possible radiation trapping may give additional advantage for reducing energy loss from such high-Z targets.

I. INTRODUCTION

After decades of perseverance, laser-driven inertial confinement fusion (ICF) has recently reached the significant milestones of realizing both burning plasma and ignition with a target gain of G > 1 [1–3]. This fantastic breakthrough on the National Ignition Facility (NIF) [4] has brought back the prospect of commercializing fusion energy through laser-driven ICF, even though this breakthrough has only been demonstrated with the laser indirect-drive (LID) scheme. In the LID scheme, laser energy needs to be first converted into thermal x-rays in a gold hohlraum to indirectly drive the fusion capsule. This leads to smoother drive but lower laser energy coupling efficiency to the imploding deuterium-tritium (DT) capsule so as to the final hot spot, thereby resulting in only a moderate gain of G $\leqslant$ ~10 for LID target design *even* in codes with a reasonable laser energy ($\sim$ 2 MJ). Thus, the target complexity and its limit on target gain may make the LID scheme less practical for the inertial fusion energy application and for the pursuit of significantly high neutron yields towards other high-energy-density applications, unless the efficiency from electricity plug to laser is significantly improved.

Different from LID, laser-direct-drive (LDD) is another scheme for laser fusion [5-8], in which a millimeter-sized capsule, consisting of a thin DT-ice layer covered by an ablator layer made of low-Z materials (*e.g.*, polystyrene, Be, carbon, *etc.*), is directly irradiated by high-power laser beams. The advantage of LDD over LID is that it can couple at least twice more laser energy to the imploding shell, even though other challenges exist for LDD (discussed in below). In the LDD scheme, high-intensity (10^{14} – 10^{15} W/cm^2) laser irradiation on target can heat and ablate the outer layer of the capsule, which creates large ablation pressure of $P > 100$ Mbar to drive the remaining target to implode. Given a significant acceleration in a short

amount of time by laser ablation, the imploding dense DT shell can reach very high velocities ($v_{imp} > 3.7 \times 10^7$ cm/s) so that it can attain tens of kilo-joule kinetic energy. Once such an energetic DT-shell stagnates against the DT-gas core, it converts part of its kinetic energy into the thermal energy of the core, forming the so-called "*hot-spot*" through the usual *pdV* work and the ablation of inner side of the DT shell. The rest of the kinetic energy is to compress the dense DT layer to high densities for the needed inertial confinement. In such conventional LDD target designs [9-15], all of the low-*Z* ablator materials will get ablated away before the capsule comes to stagnate. Thus, during the stagnation stage the dense DT-shell is *pushing* on the hot DT core. This type of *DT-push-on-DT* targets require careful timing of shocks and maintaining the DT-shell on a low-entropy state (low-adiabat) to be compressible. Generally speaking, such *DT-push-on-DT* implosions need to have the in-flight shell being on low-adiabat ($\alpha = P/P_F \leq \sim 3$, with P being pressure of the shell and P_F being the Fermi degeneracy pressure of the corresponding electron density); They also require to have a high hot-spot convergence ($CR_{hs} > 25$) and high implosion velocity ($v_{imp} > 3.7 \times 10^7$ cm/s), for reaching ignition and target gain of $G > 1$.

These stringent requirements discussed above impose great challenges on LDD fusion with conventional *DT-push-on-DT* target designs, even though significant milestones and progresses have been continuously made over the past decade [16-20]. The most daunting task for LDD is to keep the in-flight dense DT shell on a low-entropy state for the needed compression ρR at stagnation to provide enough confinement time and large burn fraction [$f_b = \rho R/(\rho R + 7)$ with ρR in units of g/cm^2] for ignition and energy gain. However, low-adiabat implosions are susceptible to the notorious Rayleigh-Taylor instability seeded by perturbations like laser imprint [21-27], defects [28], and other non-uniformity induced mixing [29,30]. Over the past

three decades, many ideas have been proposed to render these challenges by decoupling the assembling of dense DT shell from the hot-spot formation. For example, fast ignition [31-33] separated the low-velocity DT fuel assembling from an additional fast heating to spark the burn, while shock ignition [34-37] relies on a very strong shock ($P > 300$ Mbar) to initiate the burn. Taking the similar logic, some other ideas such as shock-augmented ignition [38], double-shell targets [39-43], and multiple-shell targets [44,45] were also explored recently and/or in the past. Specifically, in the double-/multiple-shell targets for volumetric ignition, a high-Z layer (inner shell) is used to serve as the high-density *pusher* to compress the liquid DT core and to provide the high ρR (>1 g/cm^2) for confinement. Although 1-D designs of these volume-burn targets with high-Z layer(s) are promising, they are struggling to reach target gain of $G > 1$ in 2-D and 3-D simulations, even though burning plasmas are possible with direct-drive double-shell design [43]. These studies have shown that the high-Z layer in such targets does help to reduce the heat conduction loss and to partially "*recycle/trap"* the radiation loss from DT fuel. These benefits enable α-particle bootstrap heating in these double-/multiple-shell targets to occur at relatively low ion temperature ($T_i \sim 3.5$ keV) instead of ~5 keV required for *DT-push-on-DT* targets. However, the small convergence ($CR \leq 10$) of DT fuel adversely limits the ignition margin and target gain for double-/multiple-shell targets.

Taking the benefits of the high-Z layer in double-/multiple-shell targets and removing the drawback of their limited convergence, MacLaren *et al* [46] have recently proposed the concept of *pushed-single-shell* (PSS) design as an alternative to the low-Z ablator targets often considered by the laser-indirect-drive (LID) scheme. The first room-temperature PSS target implosions on NIF, using graded metal shell for LID, have shown the desired stability evidenced by the high (~35%) yield-over-simulated measurement [47]. As discussed above, the

LDD scheme can generally couple more laser energy to the imploding shell, even for the case that the cross-beam energy transfer (CBET) effect is currently limiting the energy absorption of narrow-band lasers. Given the advantages (higher hydro-efficiency and simple targets) and disadvantage (imprinting and laser plasma instability) of the LDD scheme, here we intend to examine whether or not the high-Z gradient-density pusher-shell (GDPS) design could offer a viable path towards LDD fusion ignition with target gain of $G > 1$, using currently-available narrow-band driven lasers. Studies on such an alternative to conventional low-Z ablator targets is important, because the conventional *DT-push-on-DT* targets are found to have small or no margin to ignition/gain in the presence of the detrimental CBET effect in LDD. Even if CBET gets mitigated by future broad-band lasers [48], high-Z gradient-density pusher-shell (GDPS) targets could potentially provide another robust platform for high-yield applications.

In this paper, we report on our studies on GDPS target design physics based on both 1-D and 2-D radiation-hydrodynamic simulations. Similar to the case of direct-drive double-shell design [43], we are considering to use the gradient-density shell of tungsten-beryllium (W-Be) mixture by the magnetron sputtering technique [49] developed at General Atomics. This is somewhat different from the current use of Cr-Be shell in PSS implosions with LID [47]. To mitigate laser imprinting effects in LDD, we adopt an Au-coating foam layer that can be manufactured by the two-photon-polymerization (TPP) technique [50-53] with CHON resin. Overall, our results show that with a reasonable laser energy of 1.9–2.5 MJ under symmetric direct drive, these high-adiabat, low-convergence and low-velocity GDPS targets can provide ~50 MJ neutron yield in 1-D modeling, even with the notorious CBET present; Two-dimensional simulations with laser perturbations and ice roughness indicate that these targets can still reach ignition with moderate gain (up to ~10 MJ neutron yield). We explored what the physics is behind the better

target performance of GDPS implosions over conventional *DT-push-on-DT* targets. In addition, we also investigated the GDPS target implosions for the case of no CBET (e.g., using future broadband lasers), which give neutron yields up to ~20 MJ.

The paper is organized as follows: In Sec. II, we give general considerations of designing high-*Z* gradient-density pusher-shell (GDPS) targets for LDD fusion. The 1-D simulation results by *LILAC* [54] are presented in Sec. III, where we discuss the high-adiabat benefit of the high-Z pusher shell to against the usual Rayleigh-Taylor (RT) growth which is key to have a stable GDPS implosion. Two-dimensional radiation-hydrodynamic simulations of these GDPS target implosions using *DRACO* [55] are discussed in Sec. IV, in which laser perturbations, beam geometry, and DT-ice roughness are considered. The role of the Au-coated foam layer to mitigate laser perturbations is another crucial factor to make such LDD implosions less susceptible to laser imprints. Finally, we summarize the physics findings about such GDPS target designs for LDD fusion in Sec. V.

II. GENERAL CONSIDERATIONS OF DESIGNING GDPS TARGETS FOR LDD FUSION

As demonstrated by direct-drive double-shell design [43] and the recent PSS target implosion on NIF [47], the use of gradient-density shell of high-*Z* materials is essential to reduce the RT growth between the ablator layer and the pusher shell. Studies on how density gradient can make ICF implosion stable had been documented in the literature [56,57]. Similar to our choice for direct-drive double-shell target [43], we take the tungsten-beryllium (W-Be) mixture as the pusher-shell material which can be made by the magnetron sputtering technique

[49]. It has been demonstrated in target fabrication that one can continuously vary the atomic fraction of tungsten (W) from 0 to 100% in the W-Be mixture. Specifically, we consider to have W-fraction changing from 0 to 31%, corresponding to the mass density of W-Be mixtures varying from $\rho = 1.84$ g/cm^3 (pure Be) to $\rho = 9.98$ g/cm^3 ($W_{0.31}Be_{0.69}$). The W-Be pusher shell, having a thickness of 10 – 12 μm, composes of twelve different step W fractions to be practical in rad-hydro simulations. In addition to the W-Be pusher layer, there is a pure Be layer of 18 – 22 μm as the main part of LDD ablator. We choose Be as the main ablator material because it provides the better hydro-efficiency due to its high value of $< A >/< Z > = 2.25$, as evidenced in previous experiments [58-60].

To mitigate laser imprinting effects [61-70] for LDD fusion, we have employed a low-density ($\rho = 80$ mg/cm^2) foam layer of 200-μm thick, which can be made by 3-D printing through the two-photon-polymerization (2PP) technique with the CHON resin [50-53]. Using low-density foams to reduce laser imprints have bene extensively studied in both simulations and experiments [71-74]. Recent experimental results on the Omega Laser Facility indeed show a significant reduction, in particular when the foam layer is coated with a thin (~500 Å) gold layer [75-77]. To make the Au-coating possible, an 1-μm solid CHON layer is 3-D printed on top of the foam layer. Both the foam and the solid layer can be 3-D printed altogether using the 2PP technique [50-53]. The 3D-printed foam layer with Au-coating can be made with two semi-shells which can be assembled on top of the W-Be pusher shell. Illuminated by a weak laser picket, the thin Au-layer gives a ~100-ps soft x-ray flash, which can melt the 3D foam structures and create low-density but over-critical plasmas to prevent direct laser imprints on the solid Be surface. This mechanism is different from to the hybrid scheme for laser imprint

reduction in recent planar experiment [78], in which the first shock is produced by laser-generated soft x rays.

Finally, a cryogenic solid DT-ice ($\rho = 0.25$ g/cm^3) of 40 – 50 μm thick is layered in the backside of the pusher shell, as the fusion fuel. The core is filled with DT gas at its equilibrium density of $\rho \approx 0.64$ mg/cm^3, which is also part of the total fuel mass. For a typical design of these GDPS targets, we give the material composition, density, mass, and their radial locations in Table I. As one can see, the W-Be pusher shell has the similar mass as the DT fuel. Of course, the pusher material is not fusible; it only provides the needed "piston" to do the pdV work on the DT fuel inside. Comparing to the conventional *DT-push-on-DT* targets, the use of high-density but non-fusible pusher shell is an unavoidable sacrifice. A picture of such typical GDPS targets (diameter of $\phi \approx 3.8$ mm) is displayed as an insert in Fig. 1, where the on-target laser intensity is plotted as a function of time. Overall, we have limited the peak laser intensity to $\sim 6 \times 10^{14}$ W/cm^2 to reduce the potential hot-electron preheat through the two-plasmon decay and stimulated Raman scattering processes [79-82], even though the high-Z pusher layer can possibly tolerate more electron preheat than DT. It is noted that the first weak laser picket, shown in Fig. 1, is applied to generate soft x-ray flash by the Au-coating for melting the 3D foam structure. That goal has preliminarily demonstrated in our most recent planar experiments [77]. The ~3-ns temporal gap between the first weak picket and the main laser picket is to allow the melted foam structures to homogenize before the first shock is launched. The main pulse consists of a mid-intensity step pulse, by which we intentionally put the pusher shell in a very high adiabat ($\alpha = 6 - 10$) with three shocks to mitigate the RT instability (discussed in below). The total laser energy for this pulse shape is about ~1.9 MJ, even though some of our design studies explore higher driven laser energies up to ~2.5 MJ. It

is noted that this range of laser energies is within the current (or near-future enhanced) capability on NIF.

III. 1-D *LILAC* SIMULATIONS OF GDPS TARGET IMPLOSIONS

With the gradient-density pusher-shell (GDPS) target and laser pulse shape designed above, we have first performed the one-dimensional radiation-hydrodynamic simulation of its implosion, by using the 1-D lagrangian code *LILAC* [54] developed for LDD at Laboratory for Laser Energetics (LLE). The state-of-the-art physics models have been invoked in our rad-hydrodynamic simulations. They include the first-principles equation-of-state (FPEOS) tables for materials of DT [83-85], Be [86], and CHON [87], while W-Be mixtures are modelled by mixing Be-FPEOS with SESAME-EOS for tungsten and Au by the SESAME table [88]; For thermal transport the iSNB nonlocal model [89] is used; And radiation transport uses the 48-group diffusion model with first-principles opacity table (FPOT) [90] for DT, astrophysics opacity table [91] for Be, and averaged-ion based NLTE opacity tables [92] for mid-/high-Z materials of W-Be, CHON, and Au. Finally, the inverse-Bremsstrahlung laser absorption also invokes the experiment-benchmarked and ray-based stimulated Brillouin scattering (SBS) model to simulate the cross-beam energy transfer (CBET) effect [93,94]. To partially reduce the CBET effect, we have optimized the ratio of laser beam size to the target size, $R_{beam}/R_{target} = 0.8$, resulting in a total laser absorption around ~80%.

The LILAC simulation results are shown in Figs. 2–4 for the GDPS target design displayed by Fig. 1. In Fig. 2 the Lagrangian layer (radial) positions are plotted as a function of time. It indicates that the first small laser picket “burns” off the 1-μm solid CHON and the 50-nm Au

coating, with a weak shock (~1 Mbar) crushing through the CHON foam layer before the main picket starts at t = 4 ns. Such *pre-plasmas* are therefore formed to help smoothing laser perturbations. When the main laser picket comes to interact with the target, it launches a strong shock (~20 Mbar) in the homogenized CHON foam at $R \approx 1850$ μm which is ~ 150 μm distance away from the solid-Be surface. This avoids the direct laser perturbations being imprinted onto the solid target surface; It also provides a certain distance for possible healing of shock modulation when it propagates upward the gradient-density plasmas. Figure 2 shows that once the CHON foam is ablated away at ~7.5 ns, the Be layer starts to serve as the high hydro-efficiency ablator. The efficient ablation drives the remaining target, consisting of the W-Be pusher shell and the DT layer, to implode for the rest of ~7 ns. The W-Be shell pushing on the DT layer stagnates at $t \approx 14.5$ ns; then the ignition/burn follows.

To further explore this type of GDPS target implosion, we plot the in-flight shell profiles of density (blue/solid line) and adiabat (red/dashed line) as a function of radius in Fig. 3(a), at $t = 10.8$ ns when the shell converges to roughly two thirds of its initial radius. One interesting feature for this type of LDD target is that the high-density W-Be pusher shell can be placed on a very high adiabat ($\alpha \approx 8$), while the main DT mass can have a low entropy state ($\alpha \approx 2 - 3$). In addition, the ablator layer of Be has a extremely high adiabat ($\alpha \approx 50$), which is outside the plotting range in Fig. 3(a). This feature is very important to allow the GDPS implosion to be less susceptible to the RT instability, as higher adiabat at ablation front generally favors the ablative stabilization of RT growth [95-97]. *DRACO* simulations to be discussed in next section demonstrate the benefit of such an extreme adiabatic "shaping". Figure 3(b) shows the implosion velocity *versus* time, as well as the areal density (ρR) history. It indicates that this type of GDPS target only needs a relatively low implosion velocity of $v_{imp} \approx 281$ km/s to

reach ignition, which is ~30% lower than the convention *DT-push-on-DT* target for which a minimum implosion of $v_{imp} \approx 370$ km/s is required. The lower implosion velocity needed for GDPS targets can also relax the shell acceleration for a smaller RT growth rate. The reason for GDPS targets requiring only a lower implosion velocity to ignite is due to its high initial density *(e.g.,* $\rho_0 \approx 10$ g/cm^3 for the case discussed here), which is much larger than a typical *DT-push-on-DT* target. At the end, the ignition-relevant kinetic energy ($K > 50$ kJ) of the in-flight shell, $\sim \rho v_{imp}^2$, can be attained with a relatively lower velocity for high-density GDPS targets. At stagnation, such a slow GDPS implosion can still give a very high total compression $\rho R \sim 2$ g/cm^2, as shown by the dashed curve in Fig. 3(b). The *LILAC*-predicted areal density of DT-fuel (including the hot-spot and DT-shell) can reach over ~600 mg/cm^2, even for simulation with CBET on.

Finally, the density and ion temperature conditions are illustrated in Fig. 4 for the GDPS implosion at stages of stagnation [Fig. 4(a)] and peak neutron production [Fig. 4(b)]. One can see that during the stagnation the W-Be shell pushes on the DT layer to against the hot-spot DT core, which compresses the DT layer to a relatively high density ($\rho \sim 300$ g/cm^3) and does the usual pdV work to the DT core to heat it up to a peak ion temperature of $T_i \approx 10$ keV. The resulting hot spot, having a large core radius, $R_{hs} \approx 75$ μm, is dense ($\rho \sim 40$ g/cm^3) and hot enough to bootstrap heating by its DT-fusion produced alpha particles. Figure 4(b) shows that the initiated burn wave depletes the compressed DT shell and make the whole DT fuel a burning hot core reaching a high temperature of $T_i \approx 30$ keV at this time, while it's still confined by the W-Be pusher shell. The produced huge pressure ($P \sim 2000$ Gbar) launches a extremely strong shock to compress the W-Be pusher layer to densities over ~4000 g/cm^3. The large pusher-shell ρR (~1.1 g/cm^2) provides enough confinement time (~100 ps) for the DT

core to burn and generate high neutron yield of $Y \approx 2.08 \times 10^{19}$ (corresponding to ~58 MJ energy) from the 1-D *LILAC* simulation. Table II summarizes the overall performance of the GDPS target from *LILAC* prediction, in which all quantities in the bracket "<···>" are neutron averaged. Different from the conventional *DT-push-on-DT* targets, these GDPS targets can ignite at relatively lower hot-spot convergence ratio of CR_{hs}~22, while the pusher shell needs only a convergence ratio of CR_{PS}~17. In addition, the LILAC simulation with no CBET for the same GDPS target is also included in Table II for comparison. Overall, the no-CBET case does somewhat better than the CBET case; In particular, the implosion velocity can be increased by ~10% which gives more margin for ignition and gain in 2-D simulations (discussed in below).

Besides the 1.9-MJ design, we have also explored what might happen if one may have slightly higher driven laser energy. To that end, we examined a similar target design with 2.5-MJ laser energy. The target size and composition are very similar to those of the 1.9-MJ target discussed above, except that the W-Be pusher layer is slightly thicker (changing from 10 μm to 12 μm); the thickness of Be ablator layer is increased by 4 μm to 22 μm; and the DT-ice layer is reduced from 45-μm to 40-μm thick. In addition, the laser pulse is extended to a total pulse duration of 13.5 ns. The *LILAC* predictions of this GDPS targets are summarized in Table III. Overall, we saw similar 1-D performance as that of the 1.9-MJ target, while the 2-D *DRACO* simulations of this 2.5-MJ target show more margin for ignition and gain (discussed in next section).

IV. 2-D *DRACO* SIMULATION RESULTS

Given the promising 1-D target designs discussed above, we shall examine if such GDPS targets can survive the nominal laser and target perturbations in two-dimensional radiation-

hydrodynamic simulations. For this purpose, we have performed *DRACO* simulations of GDPS target implosions, including perturbations from laser port geometry (taking the 60-beam OMEGA configuration as an example), laser imprint modes up to $l_{max} = 100$, and the long-wavelength roughness of $\sigma_{rms} = 1$ μm at the back surface of DT-ice layer. Each laser beam has a super-gaussian (SG-5) spatial shape that covers only 80% of the target diameter. To see the worst scenario, we have turned off the smooth by spectral dispersion (SSD). The target is discretized on a 2-D grid of 650×350 zones on the cylindrical *R-Z* plane, while the symmetry axis is around the *Z* axis. Three-dimensional ray tracing [94] is applied to model the laser deposition with the choice of invoking CBET or not. The *DRACO* runs are using the Lagrangian mode with rezoning; The same state-of-the-art physics models used in *LILAC* are also employed in these *DRACO* simulations with/without invoking CBET. These results are presented in the following Figs. 5–8, for the case of 1.9-MJ laser energy.

Figure 5 shows the density contours during the acceleration stage of the GDPS target implosion at times of (a) $t = 11$ ns, (b) $t = 12$ ns and (c) $t = 13$ ns, with CBET is present. One sees that the pusher shell's density gets perturbed as the implosion proceeds, which is due to the usual Rayleigh-Taylor instability growth of laser and target perturbations. Since the in-flight pusher shell is in very high adiabat [$\alpha \approx 8$, see Fig. 3(a)], the RT growth is moderate so that the shell does not break up as shown by Fig. 5(c). The right panels of Fig. 5 illustrate situations at the corresponding times in the case of no-CBET. Apparently, the no-CBET case gives more laser absorption that drives the shell to move ~10% faster than the CBET simulation. As a consequence, Figs. 5(d)–5(f) indicate that the target is converging to a smaller radius at the same corresponding times; the perturbations are growing more due to the larger acceleration. This can be further seen in Fig. 6 where the root mean square (σ_{rms}) of areal-density (ρR)

modulation of the imploding target is plotted as a function of time. The slope of $\sigma_{\mathrm{rms}}(\rho R)$ is larger for the no-CBET case. At the end of acceleration ($t = 13$ ns), the no-CBET simulation gives twice more modulation of shell's areal density: $\sigma_{\mathrm{rms}}(\rho R) \approx 16$ mg/cm^2 (no-CBET) *vs.* $\sigma_{\mathrm{rms}}(\rho R) \approx 8$ mg/cm^2 (CBET). The corresponding areal densities are ρR = 121 mg/cm^2 (no-CBET) and ρR = 87 mg/cm^2 (CBET) at this time, respectively.

After the laser pulse ends at $t = 13$ ns, the imploding shell coasts in with spherical convergence. Once the return shock from the hot spot reaches the dense shell, the target starts to decelerate. Two density contour plots are made in Fig. 7 for the deceleration phase of the two GDPS implosion simulations, with/without CBET. Instead of plotting them at the same time, we illustrate their difference at the shell converges to the similar radius. As shown by Fig. 7, the shell is moving faster by 350 – 400 ps in the no-CBET simulation when compared to the CBET case. The strong RT growth during the deceleration phase of last ~500 ps before stagnation is evident by the steep increase of $\sigma_{\mathrm{rms}}(\rho R)$ shown in Fig. 6 (before its peak). Consequently, the density "spikes" from the pusher shell are developed, which push on the dense DT as well as the hot spot [see Figs. 7(b) and 7(d)]. Fortunately, these deceleration-phase RT growth does not completely quench down the ignition/burn in the hot spot. As shown by Figs. 8(a) and 8(b), the contours of density (upper) and ion temperature (down) are plotted at the start of the burn-wave propagation, for CBET and no-CBET cases respectively. The results show that despite of the significant deceleration RT growth the hot spot is dense and hot enough to initiate the burn, even when CBET is present in *DRACO* simulation. As one expects, the ion temperature of $T_i \approx 20$ keV in Fig. 8(b) is higher in the no-CBET simulation due to its ~10% higher implosion velocity of ~310 km/s (*vs.* ~281 km/s with CBET). Figure 8 also indicates that for these GDPS targets there is a relatively large clean volume of DT fuel ($\phi \approx 120$ μm) for the burn to sustain,

even though the large deceleration-phase RT growth exist unavoidably. The high-Z layer does confine the heat and let the burn going on for ~100 ps. At the end, almost half of the dense DT layer gets burned off, which leads to moderate neutron production and energy gain.

The target performance predicted by the two *DRACO* simulations, with and without CBET, are summarized in Table IV. Compared to the 1-D performance, the nominal laser and target perturbations invoked in *DRACO* simulations have certainly degraded the GDPS implosions from their 1-D predictions. In particular, these perturbations have quenched the ion temperatures from the 1-D predicted 40~50 keV down to just 10~15 keV. Three effects contribute to the observed ion temperature reduction: (1) The density-perturbed pusher shell does not convert its full kinetic energy to the thermal energy of the hot spot; Instead, some of the kinetic energy is partitioned into the unwanted residual motion of DT fuel; (2) The perturbations increase the surface area between hot DT fuel and the cold high-Z pusher, and the cold spikes of the high-Z pusher cool the DT temperature; and (3) the confinement time is effectively reduced due to the fast expansion of the low-density portion ("bubbles") of the pusher shell. Nevertheless, these targets can still give 4~10 MJ neutron yield in these *DRACO* runs. Some additional optimizations, for example by increasing the density-gradient scale-length of the pusher shell in the DT-pusher interface, would help to reduce the deceleration RT growth for enhancing the GDPS target performance.

Finally, *DRACO* simulations for the GDPS target design with 2.5 MJ driven laser energy (Table III) are displayed by Fig. 9. Similar to Fig. 8, density and ion-temperature contour plots are made for both CBET and no-CBET cases, respectively in Figs. 9(a) and 9(b) at the burn-wave starts to propagate. Compared to the 1.9-MJ case, the ion temperatures are generally higher for

the 2.5-MJ drive, due to more kinetic energy available for the hot-spot assembling. The stronger bootstrap heating increases the neutron-averaged ion temperatures to 14~18 keV, leading to more neutron yield. As summarized in Table V, *DRACO* simulations predict output energies in the range of 10.5~17.7 MJ, giving somewhat higher margin than the 1.9-MJ target. Overall, we find these GDPS targets are robust to ignition with the direct-drive scheme. Certainly, there are still some space for optimizing this type of GDPS targets towards high gain. For instance, optimizing the ratio of DT mass to the pusher shell mass could be further explored in future studies.

V. SUMMARY

In summary, we have performed laser-direct-drive (LDD) fusion target designs with a high-Z gradient-density pusher shell (GDPS), through 1-D and 2-D radiation-hydrodynamic simulations. These studies show that ignition with moderate gain are feasible with these GDPS targets, even when the detrimental cross-beam energy transfer (CBET) effect is still present. Compared with the conventional *DT-push-on-DT* targets, the robustness of such GDPS implosions can be attributed to the following facts: (1) The high-Z pusher shell can be placed on a very high adiabat ($\alpha = 6 - 10$), while the DT fuel may still be in a low-entropy state; (2) The GDPS target ignition only needs a relatively lower implosion velocity of $v_{imp} = 250 - 300$ km/s, which can be ~30% lower than the minimum implosion velocity ($v_{imp} \sim 370$ km/s) required for conventional *DT-push-on-DT* targets; (3) These GDPS implosions only require a relatively smaller convergence ($CR_{hs} \sim 22$ & $CR_{PS} \sim 17$) to ignite; and (4) the high-Z layer

serves as a heat insulator to reduce thermal conduction loss, plus the possible radiation "recycling/trapping" by the high-Z pusher. Two-dimensional *DRACO* simulations show that ignition with producing neutrons of 4~10 MJ energy could be possible with a driven laser of 1.9~2.5 MJ in symmetric LDD configuration, even when CBET is still present. Once CBET gets mitigated in future facilities, these GDPS targets can have an even larger margin, which can possibly give 10~20 MJ neutron yields for the same laser energy. Optimization through gradient-density shaping might further reduce the deceleration-phase RT growth, leading to enhanced target performance.

Acknowledgment

This material is based upon work supported by the Department of Energy National Nuclear Security Administration under Award Number DE-NA0003856, the University of Rochester, and the New York State Energy Research and Development Authority.

This report was prepared as an account of work sponsored by an agency of the U.S. Government. Neither the U.S. Government nor any agency thereof, nor any of their employees, makes any warranty, express or implied, or assumes any legal liability or responsibility for the accuracy, completeness, or usefulness of any information, apparatus, product, or process disclosed, or represents that its use would not infringe privately owned rights. Reference herein to any specific commercial product, process, or service by trade name, trademark, manufacturer, or otherwise does not necessarily constitute or imply its endorsement, recommendation, or favoring by the U.S. Government or any agency thereof. The views and opinions of authors expressed herein do not necessarily state or reflect those of the U.S. Government or any agency thereof.

References

1. A. B. Zylstra, O. A. Hurricane, D. A. Callahan *et al.,* Nature **601**, 542 (2022).
2. H. Abu-Shawareb, R. Acree, P. Adams *et al.,* Phys. Rev. Lett. **129**, 075001(2022).
3. DOE Website: https://www.energy.gov/articles/doe-national-laboratory-makes-history-achieving-fusion-ignition.
4. E. M. Campbell and W. J. Hogan, Plasma Phys. Control. Fusion **41**, B39 (1999).
5. R. S. Craxton, K. S. Anderson, T. R. Boehly, V. N. Goncharov, D. R. Harding, J. P. Knauer, R. L. McCrory, P. W. McKenty, D. D. Meyerhofer, J. F. Myatt, A. J. Schmitt, J. D. Sethian, R. W. Short, S. Skupsky, W. Theobald, W. L. Kruer, K. Tanaka, R. Betti, T. J. B. Collins, J. A. Delettrez, S. X. Hu, J. A. Marozas, A. V. Maximov, D. T. Michel, P. B. Radha, S. P. Regan, T. C. Sangster, W. Seka, A. A. Solodov, J. M. Soures, C. Stoeckl, and J. D. Zuegel, Phys. Plasmas **22**, 110501 (2015).
6. V. N. Goncharov, T. C. Sangster, R. Betti, T. R. Boehly *et al.,* Phys. Plasmas **21**, 056315 (2014).
7. S. E. Bodner, D. G. Colombant, J. H. Gardner *et al.,* Physics of Plasmas **5**, 1901 (1998).
8. A. J. Schmitt and S. P. Obenschain, Physics of Plasmas **30**, 012702 (2023).
9. S. E. Bodner, D. G. Colombant, A. J. Schmitt, M. Klapisch, Physics of Plasmas **7**, 2298 (2000).
10. B. Canaud *et al.,* Nucl. Fusion **44**, 1118 (2004).
11. S. Skupsky, J. A. Marozas, R. S. Craxton *et al.*, Phys. Plasmas **11**, 2763 (2004).
12. V. N. Goncharov *et al.,* Phys. Rev. Lett. **104**, 165001 (2010).
13. S. X. Hu *et al.,* Physics of Plasmas **17**, 102706 (2010).
14. T. J. B. Collins *et al*., Phys. Plasmas **19**, 056308 (2012).
15. V. N. Goncharov, S. P. Regan, E. M. Campbell *et al.,* Plasma Physics and Controlled Fusion **59**, 014008 (2016).

16. T. C. Sangster *et al.*, Phys. Plasmas 20, 056317 (2013).

17. S. P. Regan *et al.,* Phys. Rev. Lett. **117**, 025001 (2016).

18. V. Gopalaswamy *et al.,* Nature **565**, 581 (2019).

19. A. Lees *et al.,* Phys. Rev. Lett. **127**, 105001 (2021).

20. A. Lees *et al.,* Phys. Plasmas **30**, 012709 (2023).

21. S. E. Bodner, Phys. Rev. Lett. **33**, 761 (1974).

22. R. Ishizaki and K. Nishihara, Phys. Rev. Lett. **78**, 1920 (1997).

23. R. Ishizaki and K. Nishihara, Phys. Rev. E **58**, 3744 (1998).

24. S. P. Obenschain, D. G. Colombant, M. Karasik, C. J. Pawley, V. Serlin, A. J. Schmitt, J. L. Weaver, J. H. Gardner, L. Phillips, Y. Aglitskiy, Y. Chan, J. P. Dahlburg, and M. Klapisch, Phys. Plasmas **9**, 2234 (2002).

25. S. Fujioka, A. Sunahara, K. Nishihara *et al.,* Phys. Rev. Lett. **92**, 195001 (2004).

26. S. X. Hu, G. Fiksel, V. N. Goncharov *et al.*, Phys. Rev. Lett. **108**, 195003 (2012).

27. M. Karasik, J. L. Weaver, Y. Aglitskiy, J. Oh, and S. P. Obenschain, Phys. Rev. Lett. **114**, 085001 (2015).

28. I. V. Igumenshchev *et al.,* Phys. Plasmas **20**, 082703 (2013).

29. B. M. Haines, F. F. Grinstein, J. R. Fincke*,* Phys. Rev. E **89**, 053302 (2014).

30. B. M. Haines, R. C. Shah, J. M. Smidt *et al.,* Nature Communications **11**, 544 (2020).

31. M. Tabak, J. Hammer, M. E. Glinsky, W. L. Kruer, S. C. Wilks, J. Woodworth, E. M. Campbell, M. D. Perry, and R. J. Mason, Phys. Plasmas **1**, 1626 (1994).

32. R. Kodama, H. Shiraga, K. Shigemori *et al.,* Nature **418**, 933 (2002).

33. P. A. Norreys, R.H.H. Scott, K.L. Lancaster *et al.*, Nuclear Fusion **49**, 104023 (2009).

34. R. Betti, C. D. Zhou, K. S. Anderson, L. J. Perkins, W. Theobald, and A. A. Solodov, Phys. Rev. Lett. **98**, 155001 (2007).

35. W. Theobald, R. Nora, M. Lafon *et al.,* Phys. Plasmas **19**, 102706 (2012); W. L. Shang *et al.,* Phys. Rev. Lett. 119, 195001 (2017).

36. R. H. H. Scott *et al.,* Phys. Rev. Lett. **109**, 015001 (2012).

37. R. H. H. Scott, K. Glize, L. Antonelli *et al.,* **127**, 065001 (2021).

38. R. H. H. Scott, D. Barlow, W. Trickey, A. Ruocco, K. Glize, L. Antonelli, M. Khan, and N. C. Woolsey, Phys. Rev. Lett. **129**, 195001 (2022).

39. W. S. Varnum, N. D. Delamater, S. C. Evans, P. L. Gobby, J. E. Moore, J. M. Wallace, R. G. Watt, J. D. Colvin, R. Turner, V. Glebov, J. Soures, and C. Stoeckl, Phys. Rev. Lett. **84**, 5153 (2000).

40. B. M. Haines, J. P. Sauppe, P. A. Keiter *et al.,* Phys. Plasmas **28**, 032709 (2021).

41. H. F. Robey, P. A. Amendt, J. L. Milovich, H.-S. Park, A. V. Hamza, and M. J. Bono, Phys. Rev. Lett. **103**, 145003 (2009).

42. D. S. Montgomery, W. S. Daughton, B. J. Albright, A. N. Simakov, D. C. Wilson, E. S. Dodd, R. C. Kirkpatrick, R. G. Watt, M. A. Gunderson, E. N. Loomis, E. C. Merritt, T. Cardenas, P. Amendt, J. L. Milovich, H. F. Robey, R. E. Tipton, and M. D. Rosen, Phys. Plasmas **25**, 092706 (2018).

43. S. X. Hu *et al.,* Phys. Rev. E **100**, 063204 (2019).

44. K. Molvig, M. J. Schmitt, B. J. Albright, E. S. Dodd, N. M. Hoffman, G. H. McCall, and S. D. Ramsey, Phys. Rev. Lett. 116, 255003 (2016).

45. B. S. Scheiner, M. J. Schmitt , S. C. Hsu , D. Schmidt, J. Mance, C. Wilde, D. N. Polsin, T. R. Boehly, F. J. Marshall, N. Krasheninnikova, K. Molvig, and H. Huang, Phys. Plasmas **26**, 072707 (2019).

46. S. A. MacLaren *et al.,* Phys. Plasmas **28**, 122710 (2021).

47. E. L. Dewald *et al.,* Phys. Plasmas **29**, 052707 (2022).

48. C. Dorrer *et al.,* Optics Express **29**, 16135 (2021).

49. H. Xu, H. Huang, J. Walker, C. Kong, N. G. Rice, M. P. Mauldin, J. D. Vocke, J. H. Bae, W. Sweet, F. H. Elsner, M. P. Farrell, Y. M. Wang, C. Alford, T. Cardenas, and E. Loomis, Fusion Sci. Technol. **73**, 354 (2018).

50. O. Stein, Y. Liu, J. Streit, J. H. Campbell, Y. F. Lu, Y. Aglitskiy, and N. Petta, Fusion Science and Technology **73**, 153 (2018).

51. L. J. Jiang *et al.,* Fusion Science and Technology **70**, 295 (2016).

52. Y. Liu, J. H. Campbell, O. Stein, L. Jiang, J. Hund, Y. F. Lu, Nanomaterials **8**, 498 (2018).

53. D. R. Harding, S. Muller, M. Bonino, Y. F. Lu, P. Fan, and S. Huang. Laser-based microfabrication and metrology of laser-driven inertial fusion targets, *The 21st International Symposium on Laser Precision Microfabrication (LPM 2020),* Virtual, June 2020.

54. J. Delettrez, R. Epstein, M. C. Richardson, P. A. Jaanimagi, and B. L. Henke, Phys. Rev. A **36**, 3926 (1987).

55. P. B. Radha, T. J. B. Collins, J. A. Delettrez, Y. Elbaz, R. Epstein, V. Yu. Glebov, V. N. Goncharov, R. L. Keck, J. P. Knauer, J. A. Marozas, F. J. Marshall, R. L. McCrory, P. W. McKenty, D. D. Meyerhofer, S. P. Regan, T. C. Sangster, W. Seka, D. Shvarts, S. Skupsky, Y. Srebro, and C. Stoeckl, Phys. Plasmas **12**, 056307 (2005).

56. N. Metzler, A. L. Velikovich, A. J. Schmitt, and J. H. Gardner, Phys. Plasmas 9, 5050 (2002).

57. N. Metzler, A. L. Velikovich, and J. H. Gardner, Phys. Plasmas 6, 3283 (1999).

58. D. T. Michel *et al.,* Phys. Rev. Lett. **111**, 245005 (2013).

59. J. L. Kline, S. A. Yi, A. N. Simakov *et al.,* Phys. Plasmas **23**, 056310 (2016).

60. A. B. Zylstra *et al.,* Physics of Plasmas **26**, 052707 (2019).

61. V. N. Goncharov *et al*., Phys. Plasmas **7**, 2062 (2000).

62. H. Nishimura, H. Shiraga, H. Azechi, N. Miyanaga, M. Nakai, N. Izumi, M. Nishikino, M. Heya, K. Fujita, Y. Ochi, K. Shigemori, N. Ohnishi, M. Murakami, K. Nishihara, R. Ishizaki, H. Takabe, K. Nagai, T. Norimatsu, M. Nakatsuka, T. Yamanaka, S. Nakai, C. Yamanaka, K. Mima, Nucl. Fusion **40**, 547 (2000).

63. T. R. Boehly et al., Phys. Plasmas **8**, 2331 (2001).

64. A. N. Mostovych, D. G. Colombant, M. Karasik, J. P. Knauer, A. J. Schmitt, and J. L. Weaver, Phys. Rev. Lett. **100**, 075002 (2008).

65. T. Watari, M. Nakai, H. Azechi, T. Sakaiya, H. Shiraga, K. Shigemori, S. Fujioka, K. Otani, K. Nagai, A. Sunahara, H. Nagatomo, and K. Mima, Phys. Plasmas **15**, 092109 (2008).

66. V. A. Smalyuk, S. X. Hu, J. D. Hager, J. A. Delettrez, D. D. Meyerhofer, T. C. Sangster, and D. Shvarts, Phys. Rev. Lett. **103**, 105001 (2009).

67. S. X. Hu *et al.,* Phys. Plasmas **16**, 112706 (2009).

68. G. Fiksel, S. X. Hu, V. N. Goncharov, D. D. Meyerhofer, T. C. Sangster, V. A. Smalyuk, B. Yaakobi, M. J. Bonino, and R. Jungquist, Phys. Plasmas **19**, 062704 (2012).

69. S. X. Hu *et al.,* Phys. Plasmas **23**, 102701 (2016).

70. D. T. Michel *et al.*, Phys. Rev. E **95**, 051202(R) (2017).

71. R. G. Watt, J. Duke, C. J. Fontes, P. L. Gobby, R. V. Hollis, R. A. Kopp, R. J. Mason, D. C. Wilson, C. P. Verdon, T. R. Boehly, J. P. Knauer, D. D. Meyerhofer, V. Smalyuk, R. P. J. Town, A. Iwase, and O. Willi, Phys. Rev. Lett. **81**, 4644 (1998).

72. S. Depierreux, C. Labaune, D. T. Michel, C. Stenz, P. Nicholaï, M. Grech, G. Riazuelo, S. Weber, C. Riconda, V. T. Tikhonchuk, P. Loiseau, N. G. Borisenko, W. Nazarov, S. Hüller, D. Pesme, M. Casanova, J. Limpouch, C. Meyer, P. Di-Nicola, R. Wrobel, E. Alozy, P. Romary, G. Thiell, G. Soullié, C. Reverdin, and B. Villette, Phys. Rev. Lett. **102**, 195005 (2009).

73. B. Delorme, M. Olazabal-Loumé, A. Casner, Ph. Nicolaï, D. T. Michel, G. Riazuelo, N. Borisenko, J. Breil, S. Fujioka, M. Grech, A. Orekhov, W. Seka, A. Sunahara, D. H. Froula, V. Goncharov, and V. T. Tikhonchuk, Phys. Plasmas **23**, 042701 (2016).

74. S. X. Hu *et al.,* Phys. Plasmas **25**, 082710 (2018).

75. R. J. Mason, R. A. Kopp, H. X. Vu, D. C. Wilson, S. R. Goldman, R. G. Watt, M. Dunne, and O. Willi, Phys. Plasmas **5**, 211 (1998).

76. D. Batani *et al.,* Phys. Rev. E **62**, 8573 (2000).

77. J. L. Peebles *et al.,* (in preparation).

78. L. Ceurvorst *et al.,* Phys. Rev. E **101**, 063207 (2020).

79. D. T. Michel *et al.,* Phys. Rev. Lett. **109**, 155007 (2012).

80. B. Yaakobi *et al.,* Physics of Plasmas **19**, 012704 (2012).

81. M. J. Rosenberg *et al*., Phys. Rev. Lett. **120**, 055001 (2018).

82. A. A. Solodov *et al.,* Phys. Rev. E **106**, 055204 (2022).

83. S. X. Hu, B. Militzer, V. N. Goncharov, and S. Skupsky, Phys. Rev. Lett. **104**, 235003 (2010).

84. S. X. Hu, B. Militzer, V. N. Goncharov, and S. Skupsky, Phys. Rev. B **84**, 224109 (2011).

85. D. I. Mihaylov *et al*., Phys. Rev. B **104**, 144104 (2021).

86. Y. H. Ding and S. X. Hu, Phys. Plasmas **24**, 062702 (2017).

87. S. Zhang *et al.,* Phys. Rev. E **106**, 045207 (2022).

88. B. I. Bennett, J. D. Johnson, G. I. Kerley, and G. T. Rood, Los Alamos National Laboratory Report No. LA-7130, 1978.

89. G. P. Schurtz, Ph. D. Nicolaï, and M. Busquet, Phys. Plasmas **7**, 4238 (2000); D. Cao, G. Moses, and J. Delettrez, Phys. Plasmas **22**, 082308 (2015).

90. S. X. Hu *et al.,* Phys. Rev. E **90**, 033111 (2014).

91. See National Technical Information Service Document No. 197808 (W. F. Huebner, A. L. Merts, Magee, N. H., Jr., M. F. Argo, "Astrophysical Opacity Library," Los Alamos National Laboratory, Los Alamos, NM, LA-6760-M, 1977). Copies may be obtained from the National Technical Information Service, Springfield, VA 22161.

92. R. Epstein, T. J. B. Collins, J. A. Delettrez, S. Skupsky, and R. P. J. Town, Bull. Am. Phys. Soc. **43**, 1666 (1998).

93. I. V. Igumenshchev et al., Phys. Plasmas **17**, 122708 (2010).

94. J. A. Marozas, M. Hohenberger, M. J. Rosenberg, D. Turnbull, T. J. B. Collins *et al.,* Phys. Plasmas **25**, 056314 (2018).

95. N. Metzler, A. L. Velikovich, A. J. Schmitt, M. Karaski, V. Serlin, A. N. Mostovych, S. P. Obenschain, J. H. Gardner, and Y. Aglitskiy, Phys. Plasmas **10**, 1897 (2003).

96. V. N. Goncharov, J. P. Knauer, P. W. McKenty, P. B. Radha, T. C. Sangster, S. Skupsky, R. Betti, R. L. McCrory, and D. D. Meyerhofer, Phys. Plasmas **10**, 1906 (2003).

97. K. Anderson and R. Betti, Phys. Plasmas **11**, 5 (2004).

Figure Captions

FIG. 1. (Color online) The high-adiabat and low-convergence laser pulse shape and target dimensions (insert) for the laser-direct-drive, high-Z, gradient-density pusher-shell targets.

FIG. 2. (Color online) The Lagrangian layer position (radial) as a function of time that shows the entire dynamics of a laser-direct-drive high-Z gradient-density pusher-shell implosion, predicted by *LILAC* with state-of-the art models of nonlocal thermal transport, CBET, and FPEOS.

FIG. 3. (Color online) (a) The *LILAC*-predicted profiles of density (blue solid) and adiabat (red dashed) as a function of target radius, at t = 10.8 ns when shell converges to roughly two third of its initial radius. (b) The *LILAC*-predicted implosion velocity and the compression areal density ρR are plotted as a function of time.

FIG. 4. (Color online) The *LILAC*-predicted profiles of density (blue solid) and ion temperature (red dashed) *versus* radius, at (a) the stagnation time (t = 14.5 ns) and (b) the time of peak neutron production (t = 14.6 ns), respectively.

FIG. 5. (Color online) Density contour plots on the (*r,z)* plane from 2-D *DRACO* simulations of the high-Z gradient-density pusher-shell implosion, during the acceleration phase at different times of (a) *t* = 11 ns, (b) *t* = 12 ns, (c) *t* = 13 ns for simulations with CBET. The right panels of (d), (e), and (f) show another *DRACO* simulation of the same target *without* invoking CBET.

FIG. 6. (Color online) The root mean square ($\sigma_{\rm rms}$) of areal-density (ρR) modulation of the imploding target as a function of time, with/without CBET in *DRACO* simulations.

FIG. 7. (Color online) Density contour plots on the (*r,z)* plane from 2-D *DRACO* simulations of the high-Z gradient-density pusher-shell implosion during the deceleration phase. Again, the left panels are for the situation with CBET, while the right panels show the no-CBET case.

FIG. 8. (Color online) The density (ρ) and ion temperature ($T_{\rm i}$) contour plots on the (*r*,*z)* plane at the DT-plasma burning stage: (a) with CBET at $t = 14.72$ ns and (b) without CBET at $t = 14.23$ ns, for the high-Z gradient-density pusher-shell target with a driven laser energy of ~1.9 MJ.

FIG. 9. (Color online) The density (ρ) and ion temperature ($T_{\rm i}$) contour plots on the (*r*,*z)* plane at the DT-plasma burning stage: (a) with CBET at $t = 14.6$ ns and (b) without CBET at $t = 14.025$ ns, for a slightly-different high-Z GDPS target with a driven laser energy of ~2.5 MJ.

TABLE I. The composition and mass for each part of a typical gradient-density high-Z pusher shell target design.

	Materials	ρ (g/cm^3)	R_{start} (μm)	R_{end} (μm)	Mass (mg)
Core	DT (gas)	0.00064	0	1627	0.012
DT-layer	DT-ice	0.25	1627	1672	0.385
Pusher-shell	W/Be mixture	2.2 to 10.0	1672	1682	0.482
Be-layer	Be	1.84	1682	1700	1.190
Foam-layer	CHON	0.08	1700	1900	0.652
Solid-CHON	CHON	1.20	1900	1901	0.054
Au-coating	Au	19.3	1901	1901.05	0.044

TABLE II. Summary of 1-D target performance for a laser-direct-drive fusion target using high-Z gradient-density pusher shell design, with the driven laser energy of ~1.9 MJ with/without cross-beam energy transfer (CBET).

Target Performance	With CBET	No CBET
Neutron yield	2.08×10^{19} (~58 MJ)	2.25×10^{19} (~63 MJ)
v_{imp}	~281 km/s	~310 km/s
CR_{hs}/CR_{PS}	~21.7 / ~17	~22 / ~17.5
$\langle \rho R \rangle_{DT}$	0.644 g/cm^2	0.744 g/cm^2
$\langle \rho R \rangle_{shell}$	1.11 g/cm^2	1.23 g/cm^2
$\langle T_i \rangle$	41.1 keV	49.0 keV
$\langle P \rangle$	1.85 Tbar	2.74 Tbar

TABLE III. Summary of 1-D target performance for a laser-direct-drive fusion target using high-Z gradient-density pusher shell design, with the driven laser energy of ~2.5 MJ with/without cross-beam energy transfer (CBET).

Target Performance	With CBET	No CBET
Neutron yield	1.81×10^{19} (~51 MJ)	2.06×10^{19} (~58 MJ)
v_{imp}	~292 km/s	~336 km/s
CR_{hs}/CR_{PS}	~22.0 / ~16.3	~21.8 / ~16.6
$\langle\rho R\rangle_{DT}$	0.579 g/cm^2	0.673 g/cm^2
$\langle\rho R\rangle_{shell}$	1.11 g/cm^2	1.34 g/cm^2
$\langle T_i\rangle$	38.3 keV	50.6 keV
$\langle P\rangle$	1.56 Tbar	2.87 Tbar

TABLE IV. Summary of 2-D *DRACO* simulation results for the ~1.9 MJ high-Z gradient-density pusher-shell target, with/without cross-beam energy transfer (CBET).

Target Performance	With CBET	No CBET
Neutron yield	1.41×10^{18} (~ 4 MJ)	3.28×10^{18} (~9.2 MJ)
$\langle\rho R\rangle_{DT}$	0.624 g/cm^2	0.704 g/cm^2
$\langle\rho R\rangle_{shell}$	0.97 g/cm^2	1.12 g/cm^2
$\langle T_i\rangle$	10.7 keV	15.1 keV
<*Burn-volume*>	$2.47 \times 10^4\ \mu m^3$	$2.39 \times 10^4\ \mu m^3$

TABLE V. Summary of 2-D *DRACO* simulation results for the ~2.5 MJ high-Z gradient-density pusher-shell target, with/without cross-beam energy transfer (CBET).

Target Performance	With CBET	No CBET
Neutron yield	3.74×10^{18} (~ 10.5 MJ)	6.32×10^{18} (~17.7 MJ)
$<\rho R>_{DT}$	0.590 g/cm^2	0.646 g/cm^2
$<\rho R>_{shell}$	1.06 g/cm^2	1.21 g/cm^2
$<T_i>$	13.7 keV	17.5 keV
<*Burn-volume*>	$3.94 \times 10^4\ \mu m^3$	$3.71 \times 10^4\ \mu m^3$

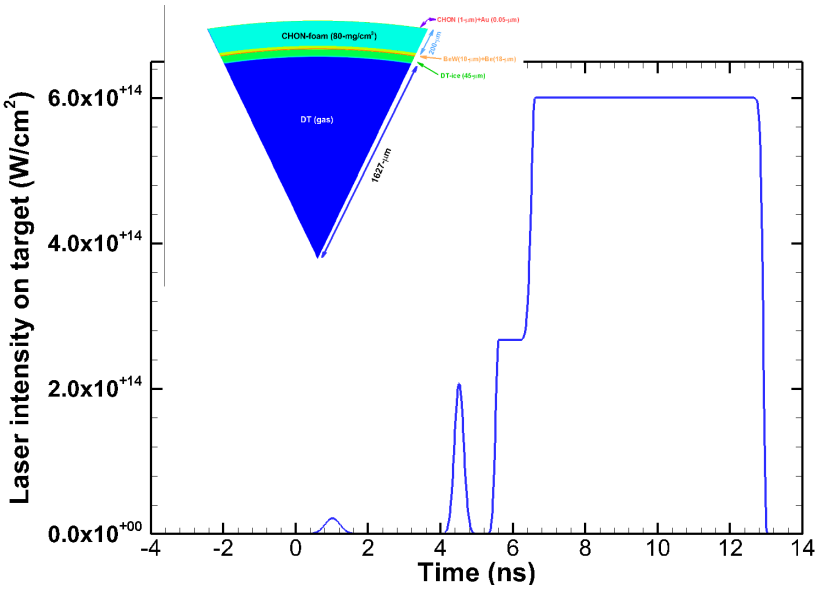

FIG. 1. (Color online) The high-adiabat and low-convergence laser pulse shape and target dimensions (insert) for the laser-direct-drive, high-Z, gradient-density pusher-shell targets.

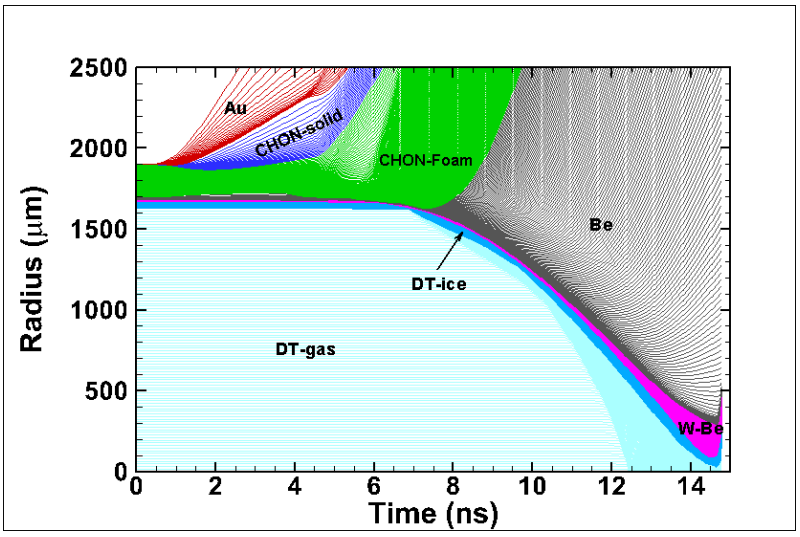

FIG. 2. (Color online) The Lagrangian layer position (radial) as a function of time that shows the entire dynamics of a laser-direct-drive high-Z gradient-density pusher-shell implosion,

predicted by *LILAC* with state-of-the art models of nonlocal thermal transport, CBET, and FPEOS.

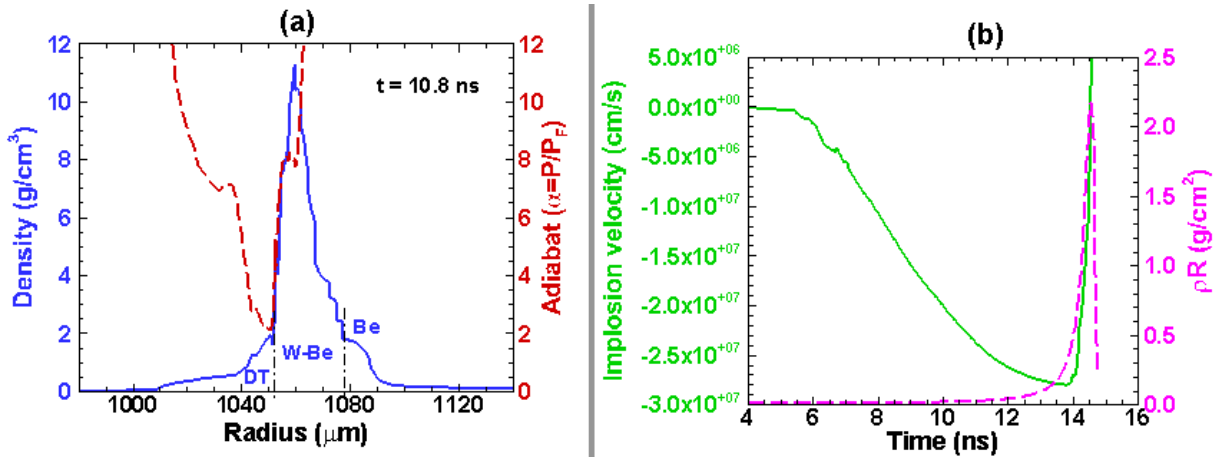

FIG. 3. (Color online) (a) The *LILAC*-predicted profiles of density (blue solid) and adiabat (red dashed) as a function of target radius, at t = 10.8 ns when shell converges to roughly two third of its initial radius. (b) The *LILAC*-predicted implosion velocity and the compression areal density ρR are plotted as a function of time.

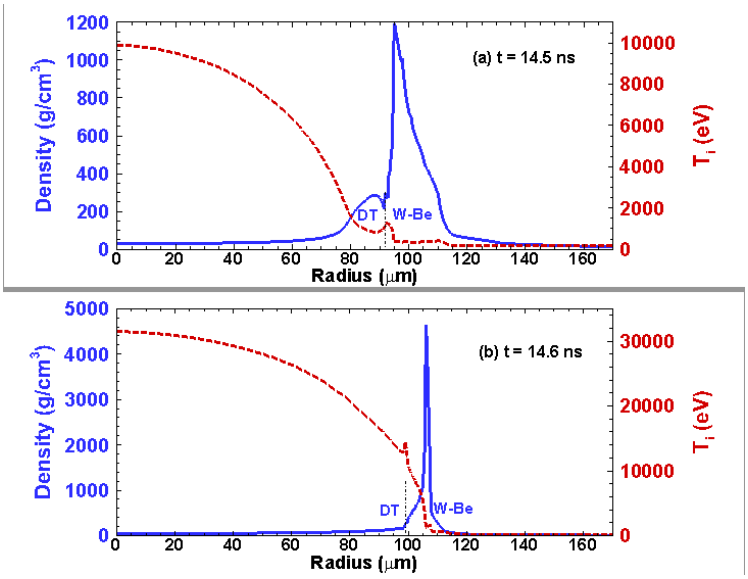

FIG. 4. (Color online) The *LILAC*-predicted profiles of density (blue solid) and ion temperature (red dashed) *versus* radius, at (a) the stagnation time (t = 14.5 ns) and (b) the time of peak neutron production (t = 14.6 ns), respectively.

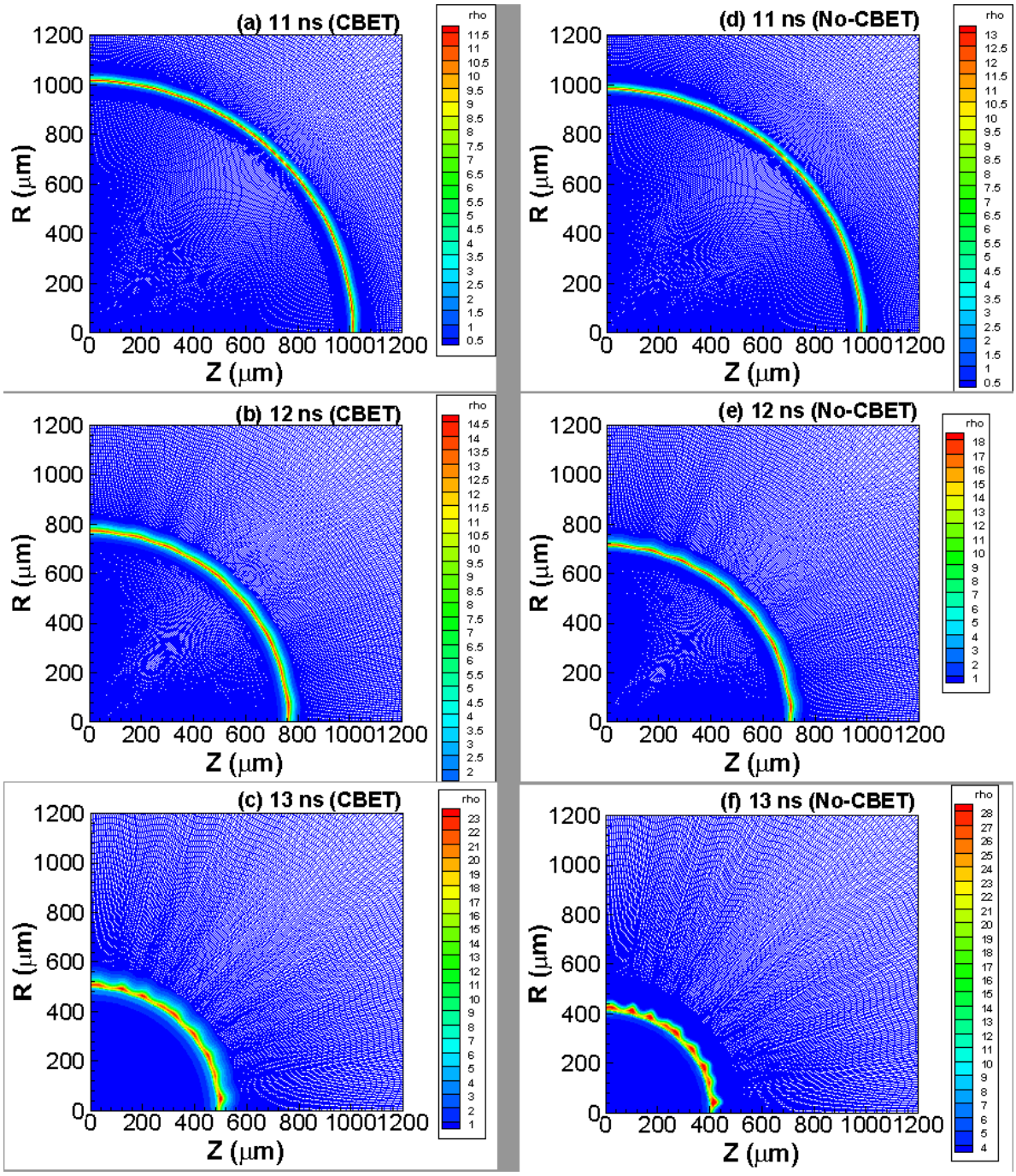

FIG. 5. (Color online) Density contour plots on the (*r,z)* plane from 2-D *DRACO* simulations of the high-Z gradient-density pusher-shell implosion, during the acceleration phase at different times of (a) $t = 11$ ns, (b) $t = 12$ ns, (c) $t = 13$ ns for simulations with CBET. The right panels of (d), (e), and (f) show another *DRACO* simulation of the same target *without* invoking CBET.

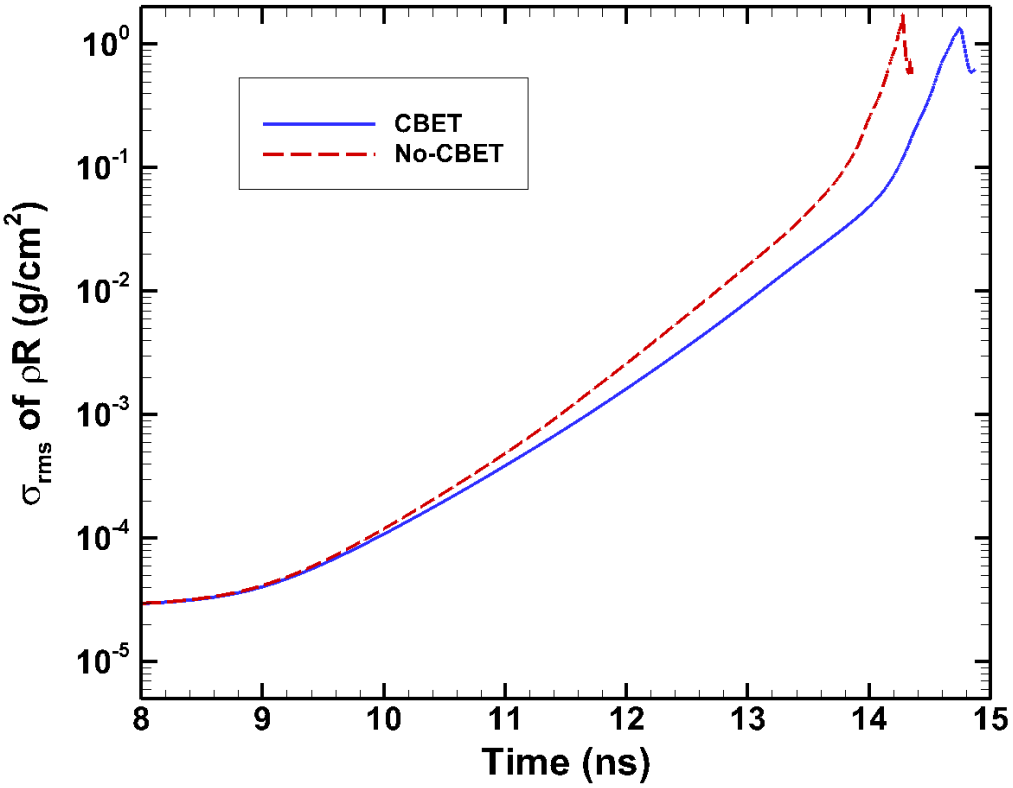

FIG. 6. (Color online) The root mean square (σ_{rms}) of areal-density (ρR) modulation of the imploding target as a function of time, with/without CBET in *DRACO* simulations.

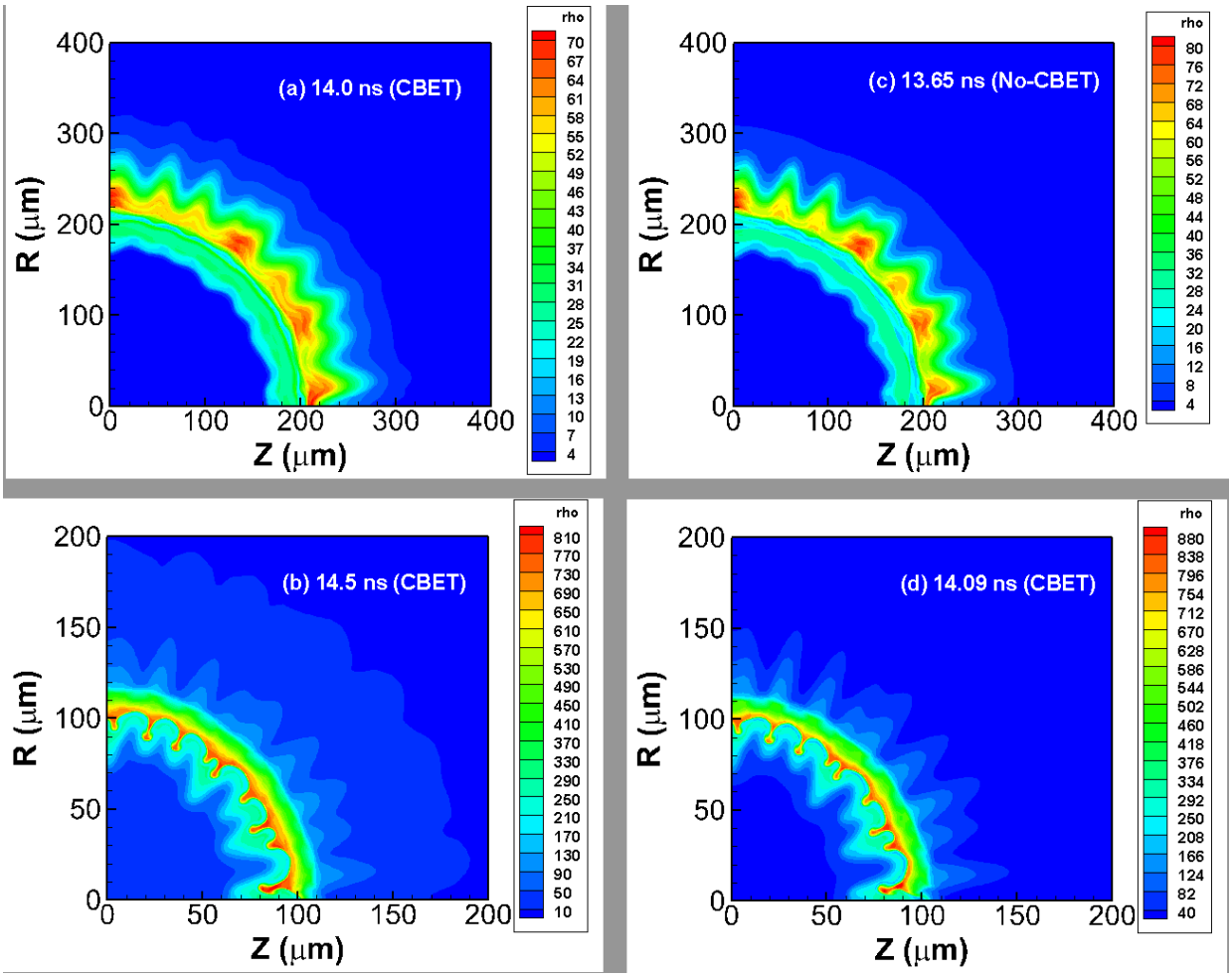

FIG. 7. (Color online) Density contour plots on the (*r,z)* plane from 2-D *DRACO* simulations of the high-Z gradient-density pusher-shell implosion during the deceleration phase. Again, the left panels are for the situation with CBET, while the right panels show the no-CBET case.

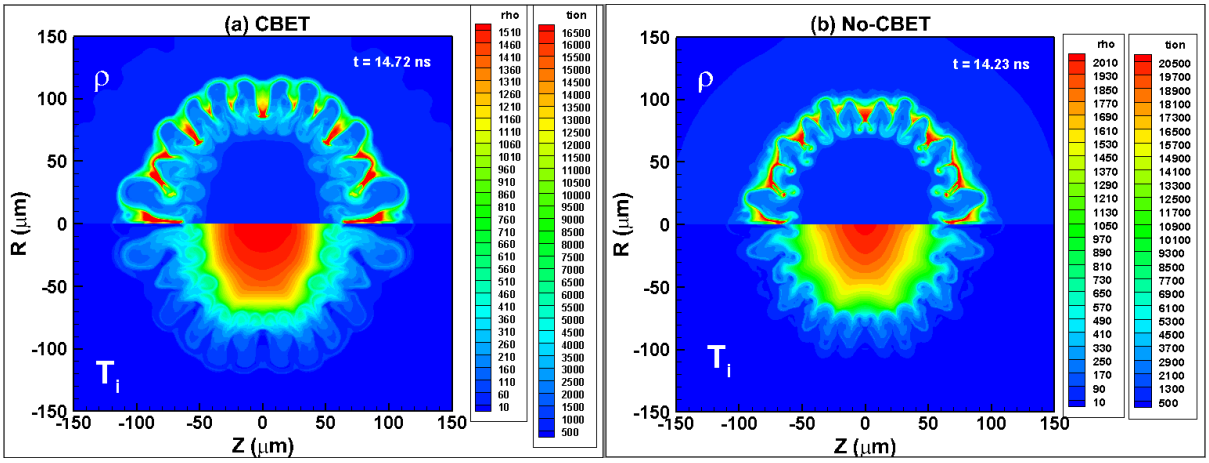

FIG. 8. (Color online) The density (ρ) and ion temperature (T_i) contour plots on the (r,z) plane at the DT-plasma burning stage: (a) with CBET at t = 14.72 ns and (b) without CBET at t = 14.23 ns, for the high-Z gradient-density pusher-shell target with a driven laser energy of ~1.9 MJ.

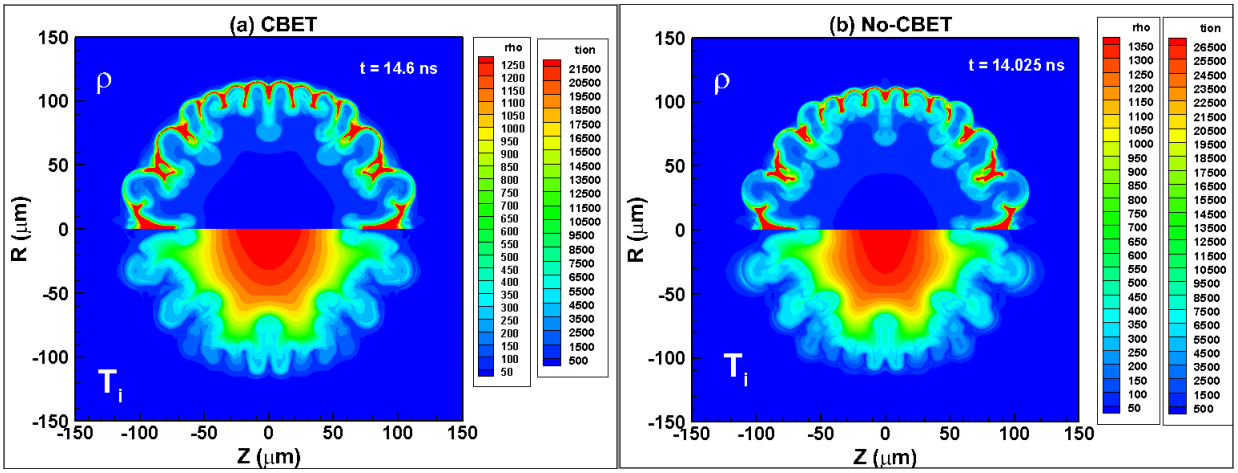

FIG. 9. (Color online) The density (ρ) and ion temperature (T_i) contour plots on the (r,z) plane at the DT-plasma burning stage: (a) with CBET at t = 14.6 ns and (b) without CBET at t = 14.025 ns, for a slightly-different high-Z GDPS target with a driven laser energy of ~2.5 MJ.